Room-Temperature Magnetic Skyrmions in Pt/Co/Cu Multilayers

Shuyu Cheng,[1] Núria Bagués,[2] Camelia M. Selcu,[1,*] Jacob B. Freyermuth,[1] Ziling Li,[1] Binbin Wang,[2] Shekhar Das,[1] P. Chris Hammel,[1] Mohit Randeria,[1] David W. McComb,[2,†] and Roland K. Kawakami[1,‡]

[1] *Department of Physics, The Ohio State University, Columbus, Ohio 43210, United States*
[2] *Department of Materials Science and Engineering, The Ohio State University, Columbus, Ohio 43210, United States*

Magnetic skyrmions are promising for next-generation information storage and processing owing to their potential advantages in data storage density, robustness, and energy efficiency. The magnetic multilayers consisting of Pt, Co, and a third metal element X provide an ideal platform to study the skyrmions due to their highly tunable magnetic properties. Here, we report the material parameters needed to achieve room-temperature skyrmions in epitaxial Pt/Co/Cu superlattices grown by molecular beam epitaxy. By tuning the Co thickness and the number of periods, the magnetic easy axis varies from perpendicular to in-plane, and skrymions are observed in the spin-reorientation transition. The magnetic properties of the Pt/Co/Cu samples are studied by magneto-optic Kerr effect (MOKE) and superconducting quantum interference device (SQUID) magnetometer measurements. Skyrmions are directly imaged by magnetic force microscopy (MFM) and Lorentz transmission electron microscopy (LTEM). The development of room-temperature skyrmions in Pt/Co/Cu multilayers may lead to advances in skyrmion-related research and applications.

Magnetic skyrmions are topologically protected spin textures that stand out as one of the strongest candidates for next-generation information storage due to their small sizes, thermal stability, and high energy efficiency [1–4]. These special spin textures originate from the complex interplay between magnetic anisotropy, dipolar interactions, applied field, and the Dzyaloshinskii–Moriya interaction (DMI). The DMI plays an important role in skyrmion formation and stabilization, as it favors perpendicular alignment between neighboring spins [5, 6]. From a material point of view, the DMI is allowed by asymmetric crystal structures, which happens in either bulk crystals that are non-centrosymmetric or interfaces that break inversion symmetry [7]. Therefore, the DMI can be categorized into bulk DMI and interfacial DMI. While the former one gives rise to Bloch skyrmions in which the spins twist in the tangential direction [8, 9], the latter one gives rise to Néel skyrmions in which the spins tumble in the radial direction [10, 11].

Since 2009, magnetic skyrmions have been discovered in a variety of materials, including B20-phase materials [8, 9, 12], two-dimensional materials [13, 14], and magnetic bilayers and multilayers [10, 11, 15, 16]. Among these materials, the Pt/Co/X (X = metallic material) magnetic multilayers have drawn much attention because the insertion of the X layers into Pt/Co superlattices generates non-canceling interfacial DMI by breaking the inversion symmetry [10, 17, 18]. Furthermore, the magnetic properties of Pt/Co/X multilayers can be vastly tuned through varying the thickness of each layer [19, 20] and the number of repetitions of Pt/Co/X [21, 22], or simply changing the element X [23, 24]. So far, the magnetic properties of Pt/Co/X multilayer systems with various metallic materials X has been reported including X = Mn [25], Ni [26], Cu [19], Ru [27], Ho [28], Ta [11], W [21], Ir [10], etc. Within a number of options for transition metal X, Cu is of particular interest for a number of reasons. Since the lattice constant of Cu is close to that of Co and Pt, it is possible to grow Pt/Co/Cu multilayers epitaxially along the Pt(111) direction [19]. This enables the layer-by-layer growth of high-quality crystalline Pt/Co/Cu multilayers using molecular beam epitaxy (MBE). It was also reported that the Pt/Co/Cu multilayers have no magnetic dead layer as compared to other materials as X layer [23]. For these reasons, Pt/Co/Cu could be a model system to investigate skyrmion properties.

In this paper, we report the material parameters needed to achieve room-temperature skyrmions in epitaxial Pt/Co/Cu multilayers. By varying the number of periods (N) and the Co thickness (t_{Co}), the magnetic anisotropy can be tuned between a perpendicular easy axis and an in-plane easy axis. We find that skyrmions form when N and t_{Co} are adjusted so that the system is in the spin-reorientation transition (SRT) between the perpendicular and in-plane magnetization states. It is notable that the presence of skyrmions is associated with a characteristic wasp-waisted shape of the macroscopic out-of-plane hysteresis loop. In addition, we observe that current pulses can help nucleate skyrmions in the SRT regime. Experimentally, the epitaxial $[\mathrm{Pt/Co/Cu}]_N$ multilayers were grown by MBE on top of a Pt(111) buffer layer grown on insulating $Al_2O_3(0001)$ substrates, which allow in-plane current pulses to be applied to the sample. The macroscopic magnetic properties of $[\mathrm{Pt/Co/Cu}]_N$ multilayers were studied using a combination of magneto-optic Kerr effect (MOKE) and superconducting quantum interference device (SQUID) magnetometry, and the skyrmions were observed using magnetic force microscopy (MFM) and Lorentz transmission electron microscopy (LTEM).

* selcu.1@osu.edu
† mccomb.29@osu.edu
‡ kawakami.15@osu.edu

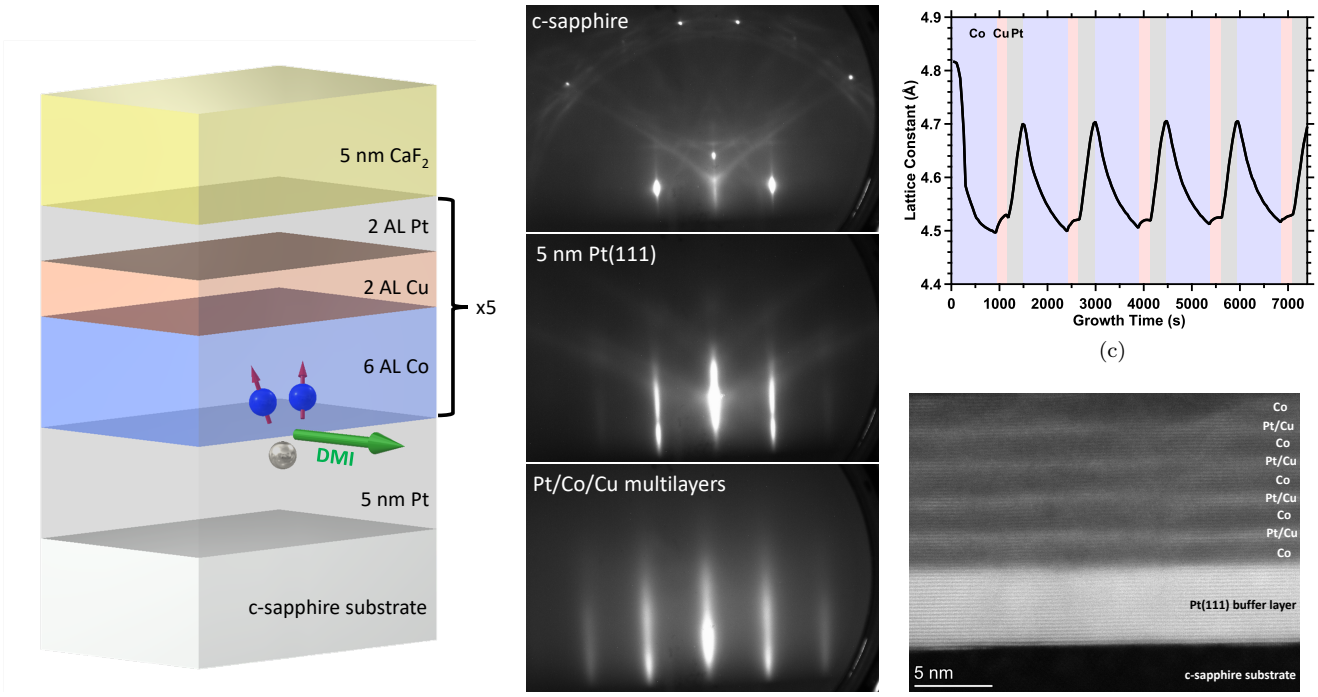

(a) (b) (c) (d)

FIG. 1. Material growth and structural characterization. (a) Schematic drawing of the sample structure. (b) *In situ* RHEED patterns during growth. Top: sapphire(0001) with the beam along the $[11\bar{2}0]$ in-plane direction. Middle: Pt(111). Bottom: $[Pt(2)/Co(6)/Cu(2)]_5$ multilayers. (c) In-plane lattice constant extracted from the RHEED streak spacing during the growth. The blue, red, and gray regions correspond to the deposition of Co, Cu, and Pt, respectively. (d) STEM-HAADF image of $[Pt(2)/Co(6)/Cu(2)]_5$ multilayers.

The $[Pt/Co/Cu]_N$ multilayers were grown on epitaxial Pt(111) buffer layers on $Al_2O_3(0001)$ substrates (MTI Corporation) using MBE. Unless otherwise noted, the structure of the multilayer samples is (bottom to top): 5 nm Pt/[6 atomic layers (6 AL) Co/2 AL Cu/2 AL Pt]$_5$/5 nm CaF_2 (hereafter $[Pt(2)/Co(6)/Cu(2)]_5$, where the sequence of the layers is from the bottom to the top, and the numbers in the parentheses represent the thickness of each layer in units of atomic layers), as shown in Figure 1a. Prior to the growth, the $Al_2O_3(0001)$ substrates were annealed in air at 1000 °C for 180 minutes and then degassed in the growth chamber at 500 °C for 30 minutes. A 5 nm Pt(111) buffer layer was epitaxially grown on the $Al_2O_3(0001)$ substrate following the recipe described in [29]. After the samples were cooled down to room temperature, $[Pt/Co/Cu]_N$ multilayers were deposited on top of the Pt(111) buffer layer by opening and closing the shutters sequentially. The growth time for each layer was determined by the growth rate which was calibrates by a quartz crystal deposition monitor. Pt was deposited from an electron-beam evaporator, while Co and Cu were deposited from Knudsen cells. The typical growth rates for Pt, Co, and Cu are 0.9 Å/min, 0.8 Å/min and 1.0 Å/min, respectively. After growth, 5 nm CaF_2 was deposited on the sample to protect the sample from oxidation. The *in situ* reflection high-energy electron diffraction (RHEED) pattern was monitored during the growth, as shown in Figure 1b. Streaky RHEED patterns indicate that the $[Pt(2)/Co(6)/Co(2)]_5$ multilayers grow epitaxially. Furthermore, the in-plane lattice constant extracted from the RHEED pattern during growth shows oscillatory behavior, with decreasing lattice constant during Co layer growth, and increasing lattice constant during Cu and Pt layer growth, as shown in Figure 1c. This oscillation of in-plane lattice constant does not decay during the growth.

The structure of the sample was confirmed by scanning transmission electron microscopy (STEM) imaging of a cross-section sample using a ThermoFisher probe corrected Themis-Z at 300 kV. The cross-section sample was prepared by Ga ion milling at 30 kV and 5 kV using a focused ion beam (FIB). Figure 1d shows a STEM high-angle annular dark field (HAADF) image of $[Pt(2)/Co(6)/Co(2)]_5$ multilayer on top of Pt buffer layer on Al_2O_3 viewed along the Al_2O_3-$[1\bar{1}00]$ axis. In Figure 1d, the $[Pt(2)/Co(6)/Co(2)]_5$ sample exhibits have well-defined layered structures. Due to atomic number (Z-) contrast in HAADF images the Co layers appear as dark layers in the STEM image, while the Pt and Cu layers appear as bright layers.

We first discuss MOKE and SQUID measurements of $[Pt(2)/Co(6)/Cu(2)]_5$ multilayers. Figure 2a shows the

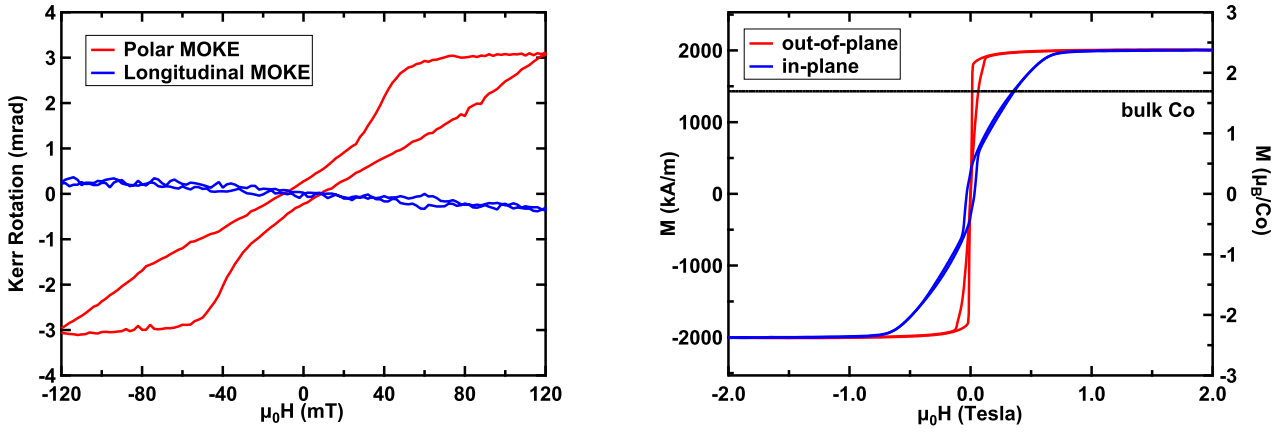

(a) (b)

FIG. 2. Magnetic characterizations of $[Pt(2)/Co(6)/Cu(2)]_5$ multilayers. (a) MOKE hysteresis loops of $[Pt(2)/Co(6)/Cu(2)]_5$ multilayers. (b) SQUID hysteresis loops of $[Pt(2)/Co(6)/Cu(2)]_5$ multilayers. The black solid line represents 1430 kA/m, which is the saturation magnetization of bulk Co.

polar (red curve) and longitudinal (blue curve) MOKE hysteresis loops of a $[Pt(2)/Co(6)/Cu(2)]_5$ multilayer. The polar MOKE hysteresis loop shows a "wasp-waisted" shape with small remanence. Although the applied magnetic field was limited to 120 mT which is not sufficient to fully saturate the sample, the hysteresis loop nevertheless captures the main magnetic characteristics of the sample. The wasp-waisted shape of the hysteresis loop is similar to that of Pt/Co/Cu multilayers near the SRT in which the magnetic stripe domains were observed [19]. Meanwhile, the longitudinal MOKE hysteresis loop shows almost linear behavior in 120 mT range, with a much smaller magnitude compared to polar MOKE. The response to external magnetic fields where the magnetization is easier to polarize out-of-plane compared to in-plane is due to the presence of perpendicular surface magnetic anisotropy from the Pt/Co interfaces.

The results from SQUID measurements of $[Pt(2)/Co(6)/Cu(2)]_5$ are shown in Figure 2b. The out-of-plane hysteresis loop (red curve) shows a similar shape to the polar MOKE loop, with low remanence and a saturation field of 192 mT, while the in-plane hysteresis loop (blue curve) saturates at $\sim$ 0.5 Tesla. We note that the the saturation magnetization of $[Pt(2)/Co(6)/Cu(2)]_5$ multilayers is larger than the bulk Co value (1430 kA/m) [30] by the amount of $\Delta M_{Co} =$ 580 kA/m. This comes from the extra magnetic moment of Pt induced by the magnetic proximity effect, which has been reported in Pt/Co multilayers [31]. To quantify this effect, we calculate the magnetic moment of Pt from the following formula [31]:

$$\Delta M_{Co}\, t_{Co} = M_{Pt}\, t_{Pt} \qquad (1)$$

By substituting $t_{Co} = 6.1$ nm and $t_{Pt} = 7.3$ nm into Eq. 1, we get $M_{Pt} = 0.84\,\mu_B$/Pt.

To investigate how the magnetic properties of [Pt/Co/Cu] multilayers depend on the material parameters, we systematically varied the Co thickness and the number of periods N. For these studies, we maintained a constant thickness of 2 AL for the Pt and Cu layers.

Beginning with the Co thickness, we synthesized a sample series of with t_{Co} = 4, 5, 6, 7, 8 and 9 AL for a fixed number of periods $N = 5$. Representative polar (red curve) and longitudinal (blue curve) MOKE loops are shown in Figure 3a. At a low Co thickness of 4 AL (sample I), the polar loop is square with a large remanence while the longitudinal loop has a small signal with no remanence. This indicates a perpendicular (out-of-plane) magnetic easy axis. As t_{Co} increases, the polar MOKE hysteresis loop evolves to a wasp-waist shape with low remanence for $t_{Co} = 6$ AL (sample III), and eventually to almost linear with negligible hysteresis and zero remanence for $t_{Co} = 8$ AL Meanwhile, the longitudinal MOKE hysteresis loop exhibits an increasing remanence with thickness, going from zero remanence for $t_{Co} = 4$ and 6 AL to a loop with substantial remanence and sharp magnetization reversals for 8 AL. This indicates a transition to in-plane magnetization for thicker Co. This spin reorientation transition (SRT) from perpendicular magnetization to in-plane magnetization with increasing Co thickness is summarized by the horizontal points at $N = 5$ in Figure 3d, with red points signifying perpendicular magnetization, green points signifying the SRT region, and blue points signifying in-plane magnetization.

This thickness-dependent spin reorientation is understood as a competition between the perpendicular magnetic anisotropy (PMA) originating from the Pt/Co interface and the magnetic shape anisotropy favoring in-plane magnetization [32]. Since the magnetic shape anisotropy scales with the Co film thickness and the

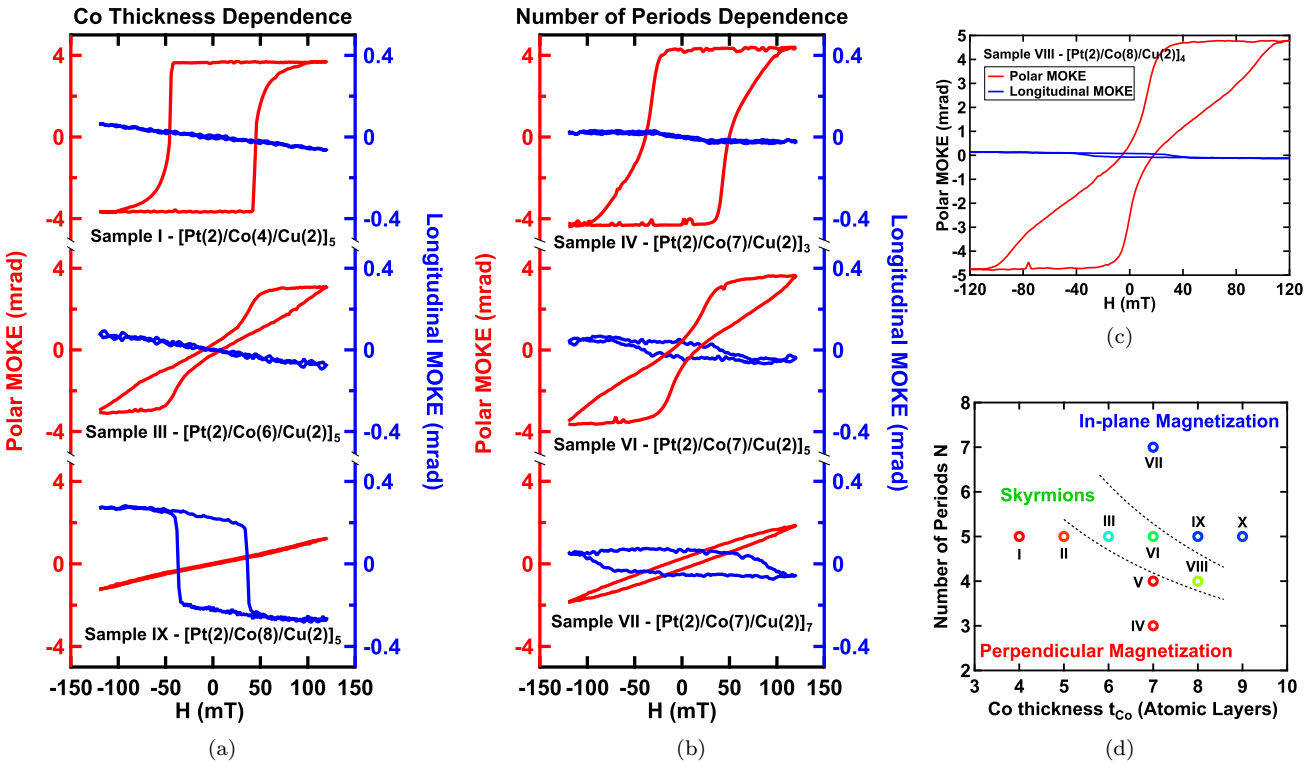

FIG. 3. Relationship between MOKE hysteresis loops and the multilayer structure. (a) Representative polar (red curve) and longitudinal (blue curve) MOKE hysteresis loops of $[Pt(2)/Co(t_{Co})/Cu(2)]_5$ multilayers with a fixed number of periods $N = 5$. (b) Representative polar (red curve) and longitudinal (blue curve) MOKE hysteresis loops of $[Pt(2)/Co(7)/Cu(2)]_N$ multilayers with fixed Co layer thickness $t_{Co} = 7$ AL. (c) Polar (red curve) and longitudinal (blue curve) MOKE hysteresis loops of $[Pt(2)/Co(8)/Cu(2)]_4$ (sample VIII). (d) Summary of the sample series. The dashed lines are guides to the eye.

Co/Pt PMA does not, larger thicknesses will favor in-plane magnetization while smaller thicknesses will favor perpendicular magnetization.

We also observe a spin reorientation transition that depends on the number of periods N of the [Pt/Co/Cu] multilayer. Interestingly, as N is increased from 3 to 7 while keeping t_{Co} fixed at 7 AL, a similar transition from perpendicular to in-plane magnetization occurs, as shown in Figure 3b. In this sample series, sample IV with 3 periods has a polar MOKE loop (red curve, top loop) with nearly 100% remanence and a longitudinal MOKE loop (blue curve, top loop) with a weak response, indicating perpendicular magnetization. For sample VI with 5 periods the polar MOKE loop (red curve, middle loop) has a wasp-waisted shape, and for sample VII with 7 periods the polar MOKE loop has a weak response (red curve, bottom loop). Meanwhile, the longitudinal MOKE loops (blue curves) for the 5-period and 7-period samples (VI and VII) develop hysteresis. This indicates that the magnetization exhibits a transition from perpendicular to in-plane as N increases.

In previous studies, both similar behavior (large N prefers in-plane) [33] and opposite behavior (large N prefers perpendicular) [22, 34, 35] have been reported for [Co/Pt] and [Co/Pt/X] superlattices. These experiments illustrate that the dependence of the magnetic easy axis on N is a complex issue, which may depend on both intrinsic interactions (e.g. anistropy, DMI, dipolar) and extrinsic factors (e.g. roughness, crystallinity). Thus, understanding the N-dependence requires further study and is beyond the scope of the current work.

Looking at the variation in magnetic anisotropy as a function of t_{Co} and N in Figure 3d shows that perpendicular magnetization is favored for low t_{Co} and low N, while in-plane magnetization is favored for high t_{Co} and high N. Since these two phases occupy opposite corners of the diagram, it is likely that the spin reorientation transition occupies a diagonal region of the diagram. To test this, we synthesized a sample with $t_{Co} = 8$ AL and $N = 4$ (sample VIII) that is to the lower-right of the two samples in the transition region (samples III, VI). Indeed, the polar and longitudinal MOKE loops for this sample (Figure 3c) confirm the wasp-waisted polar loop that signifies the spin reorientation transition region.

The magnetic properties of the samples are summarized in Table I and the hysteresis loops of each sample are shown in Section 1 of the Supplementary Material (SM).

We now focus on the samples in the transition region with wasp-waisted polar hystersis loops, indicated by the green dots in Figure 3d (and labeled "Skyrmions"). Here, we employed LTEM and MFM to image the magnetic do-

Sample ID	Co thickness t_{Co}	Number of periods N	Anisotropy
I	4	5	OOP
II	5	5	OOP
III	6	5	OOP (near SRT)
IV	7	3	OOP
V	7	4	OOP
VI	7	5	OOP (near SRT)
VII	7	7	IP
VIII	8	4	OOP (near SRT)
IX	8	5	IP
X	9	5	IP

TABLE I. Summary of the structures and magnetic properties of the samples.

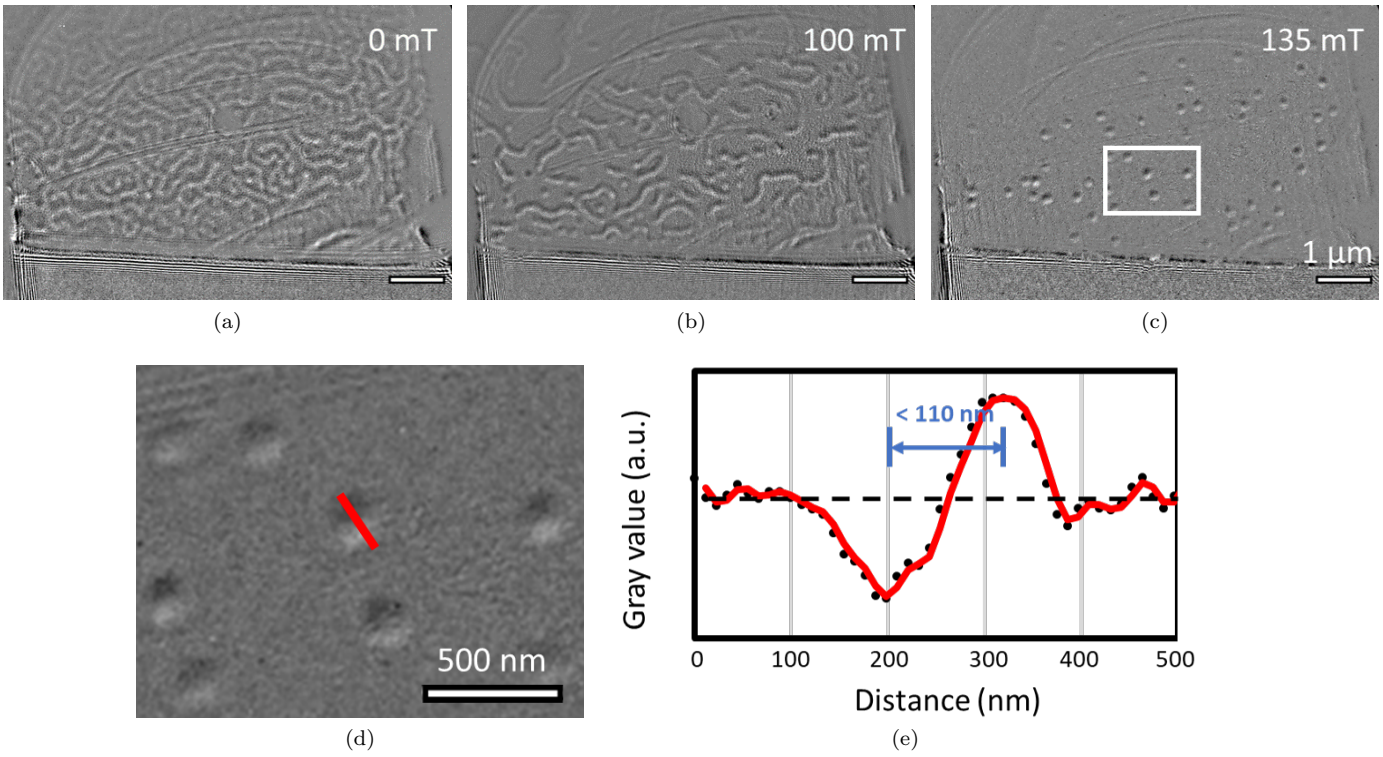

FIG. 4. LTEM images of the $[Pt(2)/Co(6)/Cu(2)]_5$ thin film with a thinned substrate. (a-c) LTEM images of the $[Pt(2)/Co(6)/Cu(2)]_5$ sample under (a) 0 mT, (b) 100 mT, and (c) 135 mT applied magnetic field. The scale bar represents 1 μm. (d). LTEM image at 135 mT after subtracting a background image taken in the field-polarized state (160 mT). The area of this image corresponds to the white box in Figure 4c. The scale bar represents 500 nm. (e). Line-cut profile of a single skyrmion along the direction of the red line in Figure 4d.

main structure and investigate the possible presence of skyrmions. For the LTEM measurements [36], focused ion beam (FIB) milling was utilized to thin the sapphire substrate, thus allowing the electron beam to transmit through the sample. Figure 4a-c shows planar-view LTEM images of a $[Pt(2)/Co(6)/Cu(2)]_5$ multilayer sample at various out-of-plane magnetic fields. The straight parallel lines are from the substrate thinning and are not due to magnetic textures. For these images, we have tilted the sample by 20° to achieve magnetic contrast for Néel skyrmions [17, 37].

Beginning at zero field (Figure 4a), we observe labyrinth magnetic domains which evolve into magnetic stripe domains when the field is ramped up to 100 mT (Figure 4b). When the field is raised to 135 mT (Figure 4c), several magnetic bubbles are observed. The image in Figure 4e has improved contrast after subtracting a background image taken in the field-polarized state at 160 mT [38].

These bubbles are identified as DMI-skyrmions of Néel type based on several considerations. First, the magnetic contrast only appears only when the sample is tilted, which is a characteristic of Néel skyrmion as the Lorentz force is tangential. Further, the bubble appears as having a positive and negative lobes, which is the expected shape for Néel skyrmion. A line-cut across the lobes,

shown in Figure 4e, establishes the size of the bubble to be smaller than 110 nm and also indicates the chirality of the bubble: the trace goes from a minima on the left to a maxima on the right while an opposite chirality would interchange left and right. Significantly, all of the bubbles exhibit the same chirality, which indicates that DMI contributes significantly to the formation of the bubble. These characteristics therefore identify the bubbles as DMI-skyrmions of Néel type.

We further investigate the magnetic domain structure and skyrmion spin textures using MFM. An advantage of MFM over LTEM is that sample preparation including substrate thinning is not required. This provides access to the as-grown magnetic properties, as substrate thinning could introduce strain. In addition, MFM measurements are compatible with devices fabricated by photolithography and electron-beam lithography. The measurements were performed in the Bruker MFM equipped with a homemade variable magnet with out-of-plane field range of -115 mT to 115 mT. The [Pt/Co/Cu] multilayers were patterned to have micron-wide device channels.

Upon investigating the three samples in the "Skyrmion" region of the phase diagram (green dots in Figure 3d), we found that skyrmions could be nucleated either using field ramp sequences or current pulses. For a $[Pt(2)/Co(6)/Cu(2)]_5$ sample (Figure 5a-c), the out-of-plane magnetic field was first set to -100 mT. Ramping to 0 mT produced labyrinth magnetic domains in the channel (Figure 5a). Increasing the field to 67 mT, the domain structure evolved to magnetic stripe domains with a lower density of domain walls (Figure 5b), consistent with the domain structures observed by LTEM (Figure 4b). As the MFM magnet is unable to reach the 135 mT needed to nucleate skyrmions, we decided to use current pulses to help nucleate skyrmions, as demonstrated previously in other materials [11, 39]. Following a single current pulse of 1.39×10^{12} A/m^2 with duration 20 ns, some of the stripe domains have broken up into isolated skyrmions (Figure 5c).

For a $[Pt(2)/Co(8)/Cu(2)]_4$ sample, the saturation field is within the range of the MFM magnet, so we investigate skyrmion nucleation by field ramping. Starting by applying a -100 mT field, we ramp up through 0 mT to a final field of 115 mT. Figure 5d-g show MFM images at representative fields. At 70 mT, the magnetic texture is dominated by stripe domains and a few skyrmions are observed. Increasing to 90 mT causes many of the stripes to nucleate into skyrmions or disappear altogether. At 100 mT, some of the skyrmions have disappeared, along with the stripes. Finally, at 115 mT, most of the sample has become field-polarized.

Additional MFM measurements establish the presence of skyrmions in a $[Pt(2)/Co(7)/Cu(2)]_5$ sample (SM Section 3).

Micromagnetic simulations were performed to try to understand the skyrmion size and its relation to various parameters. Using an exchange stiffness A_{ex} of 10 pJ/m, uniaxial anisotropy K_u of 608.5 kJ/m^3, and saturation magnetization M_S of 821 kA/m (see SM Section 4 for details), we ran simulations using MuMax3 [40] for a variety of applied out-of-plane magnetic fields and DMI strengths D including 2.15 mJ/m^2 from [41]. Results of the simulations for the $[Pt(2)/Co(6)/Cu(2)]_5$ sample are shown in Fig. 6. At zero field, the simulations show a labyrinth domain structure, consistent with both the MFM and LTEM (Fig. 6a). As the magnetic field is increased, skyrmions can be stabilized starting around 80-90 mT. Continuing to increase the field causes the skyrmions to shrink, as shown in Fig. 6c and 6d. Although the simulated values of skyrmion size are lower than the experimental values, the trend of decreasing size with increasing magnetic field is consistent for both theory and experiment. Another trend observed in the simulation is an increase of the skyrmion size with increasing values of D. These dependences of skyrmion size on D and magnetic field are in agreement with previous analytical results in Wang *et al.* [42].

In conclusion, we investigated the formation of room-temperature skyrmions in [Pt/Co/Cu] multilayers. We found that by varying the Co thickness and the number of periods N, the magnetization direction can be tuned from perpendicular to in-plane orientation. Skyrmions were observed in the spin-reorientation transition regime, where the polar MOKE loops have a characteristic wasp-waisted shape. Magnetic imaging by LTEM showed that the magnetic spin texture evolves from labyrinth domains at low perpendicular magnetic fields to isolated skyrmion spin textures at higher fields. By tilting the sample during LTEM, we verified that the skyrmions are Néel type. Since the chirality was the same for all skyrmions, this indicates the importance of interface DMI in the skyrmion formation. MFM measurements on patterned devices showed that current pulses could nucleate skyrmions at lower magnetic fields compared to nucleation by magnetic fields alone. Since the Pt/Co/Cu multilayers are epitaxial, free of magnetic dead layers, and exhibit skyrmions, this work establishes a model system for systematically investigating the properties of skyrmions.

ACKNOWLEDGMENTS

We acknowledge stimulating discussions with Denis Pelekhov. This work was supported by the DARPA TEE program under Grant No. D18AP00008. This research was partially supported by the Center for Emergent Materials, an NSF MRSEC, under award number DMR-2011876. Electron microscopy was performed at the Center for Electron Microscopy and Analysis (CEMAS) at The Ohio State University.

AUTHOR CONTRIBUTIONS

S.C. synthesized the materials and performed the RHEED, MOKE, and SQUID measurements. N.B. and

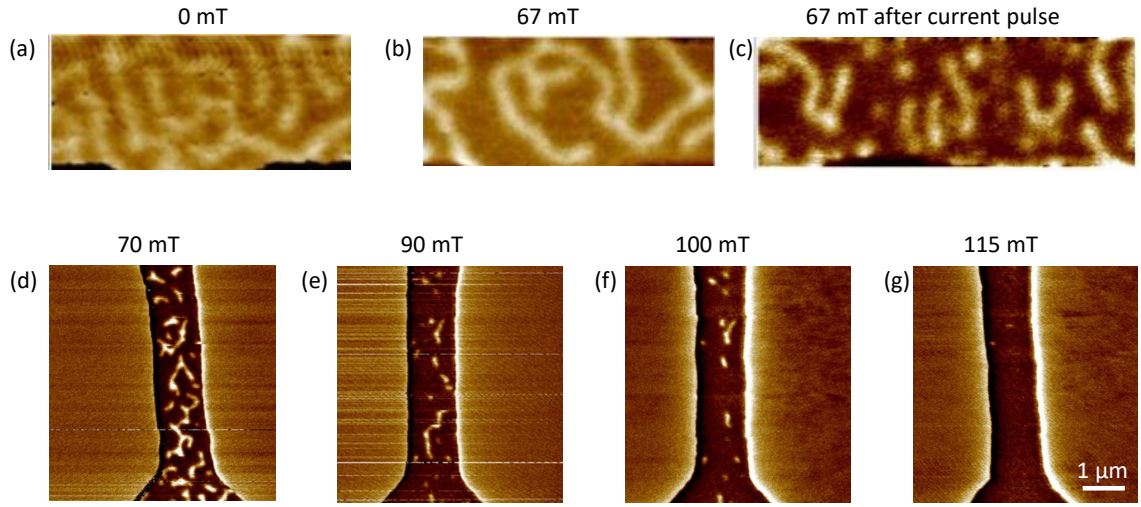

FIG. 5. MFM images of skyrmions. (a-c) For a $[Pt(2)/Co(6)/Cu(2)]_5$ sample, the magnetic field is ramped from -100 mT to 0 mT leading to labyrinth domains (a), ramping to 67 mT produces domains with lower density (b), and application of a current pulse generates isolated skyrmions (c). (d-f) For a $[Pt(2)/Co(8)/Cu(2)]_4$ sample, the magnetic field is ramped from -100 mT to 70 mT (d), 90 mT (e), 100 mT (f), and 115 mT (g). With increasing field, magnetic textures evolve from stripe domains to skyrmions to a field-polarized state.

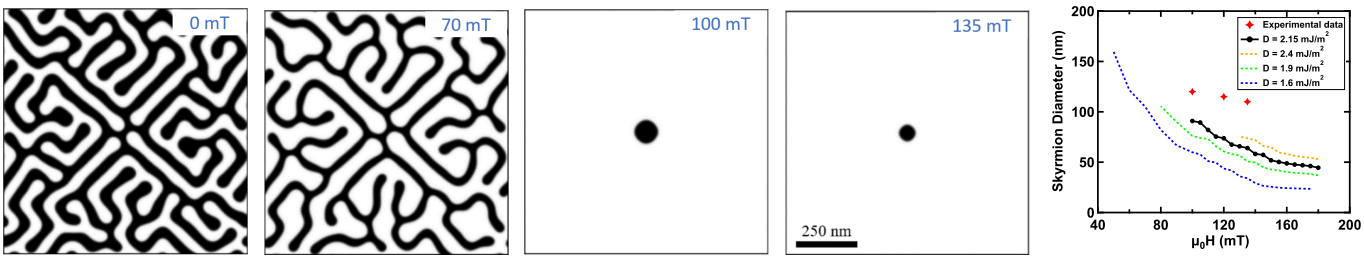

FIG. 6. Micromagnetic simulation of $[Pt(2)/Co(6)/Cu(2)]_5$ sample with (a) 0 mT, (b) 70 mT, (c) 100 mT (d) 135 mT applied field. (e). Simulated diameter of skyrmions as a function of applied field using several different DMI values. The red stars represent experimental data from LTEM measurements.

B.W. performed the TEM and LTEM measurements. C.M.S., Z.L., and S.D. performed the MFM measurements. J.B.F. and M.R. performed micromagnetic simulations. R.K.K., D.W.M, M.R., and P.C.H. conceived the study. All authors participated in data analysis and preparation of the manuscript.

[1] A. Fert, V. Cros, and J. Sampaio, Skyrmions on the track, Nature Nanotechnology **8**, 152 (2013).
[2] W. Koshibae, Y. Kaneko, J. Iwasaki, M. Kawasaki, Y. Tokura, and N. Nagaosa, Memory functions of magnetic skyrmions, Japanese Journal of Applied Physics **54**, 053001 (2015).
[3] G. Finocchio, F. Büttner, R. Tomasello, M. Carpentieri, and M. Kläui, Magnetic skyrmions: from fundamental to applications, Journal of Physics D: Applied Physics **49**, 423001 (2016).
[4] C. Back, V. Cros, H. Ebert, K. Everschor-Sitte, A. Fert, M. Garst, T. Ma, S. Mankovsky, T. Monchesky, M. Mostovoy, *et al.*, The 2020 skyrmionics roadmap, Journal of Physics D: Applied Physics **53**, 363001 (2020).
[5] I. Dzyaloshinsky, A thermodynamic theory of "weak" ferromagnetism of antiferromagnetics, Journal of Physics and Chemistry of Solids **4**, 241 (1958).
[6] T. Moriya, Anisotropic superexchange interaction and weak ferromagnetism, Physical Review **120**, 91 (1960).
[7] R. Wiesendanger, Nanoscale magnetic skyrmions in metallic films and multilayers: a new twist for spintron-

ics, Nature Reviews Materials **1**, 1 (2016).
[8] S. Mühlbauer, B. Binz, F. Jonietz, C. Pfleiderer, A. Rosch, A. Neubauer, R. Georgii, and P. Böni, Skyrmion lattice in a chiral magnet, Science **323**, 915 (2009).
[9] X. Yu, Y. Onose, N. Kanazawa, J. H. Park, J. Han, Y. Matsui, N. Nagaosa, and Y. Tokura, Real-space observation of a two-dimensional skyrmion crystal, Nature **465**, 901 (2010).
[10] C. Moreau-Luchaire, C. Moutafis, N. Reyren, J. Sampaio, C. Vaz, N. Van Horne, K. Bouzehouane, K. Garcia, C. Deranlot, P. Warnicke, *et al.*, Additive interfacial chiral interaction in multilayers for stabilization of small individual skyrmions at room temperature, Nature Nanotechnology **11**, 444 (2016).
[11] S. Woo, K. Litzius, B. Krüger, M.-Y. Im, L. Caretta, K. Richter, M. Mann, A. Krone, R. M. Reeve, M. Weigand, *et al.*, Observation of room-temperature magnetic skyrmions and their current-driven dynamics in ultrathin metallic ferromagnets, Nature Materials **15**, 501 (2016).
[12] X. Yu, N. Kanazawa, Y. Onose, K. Kimoto, W. Zhang, S. Ishiwata, Y. Matsui, and Y. Tokura, Near room-temperature formation of a skyrmion crystal in thin-films of the helimagnet FeGe, Nature Materials **10**, 106 (2011).
[13] B. Ding, Z. Li, G. Xu, H. Li, Z. Hou, E. Liu, X. Xi, F. Xu, Y. Yao, and W. Wang, Observation of magnetic skyrmion bubbles in a van der Waals ferromagnet Fe_3GeTe_2, Nano Letters **20**, 868 (2019).
[14] Y. Wu, S. Zhang, J. Zhang, W. Wang, Y. L. Zhu, J. Hu, G. Yin, K. Wong, C. Fang, C. Wan, *et al.*, Néel-type skyrmion in WTe_2/Fe_3GeTe_2 van der Waals heterostructure, Nature Communications **11**, 1 (2020).
[15] N. Romming, A. Kubetzka, C. Hanneken, K. von Bergmann, and R. Wiesendanger, Field-dependent size and shape of single magnetic skyrmions, Physical Review Letters **114**, 177203 (2015).
[16] W. Jiang, G. Chen, K. Liu, J. Zang, S. G. Te Velthuis, and A. Hoffmann, Skyrmions in magnetic multilayers, Physics Reports **704**, 1 (2017).
[17] S. McVitie, S. Hughes, K. Fallon, S. McFadzean, D. McGrouther, M. Krajnak, W. Legrand, D. Maccariello, S. Collin, K. Garcia, *et al.*, A transmission electron microscope study of Néel skyrmion magnetic textures in multilayer thin film systems with large interfacial chiral interaction, Scientific Reports **8**, 1 (2018).
[18] S. Schlotter, P. Agrawal, and G. S. Beach, Temperature dependence of the Dzyaloshinskii-Moriya interaction in Pt/Co/Cu thin film heterostructures, Applied Physics Letters **113**, 092402 (2018).
[19] L. Sun, J. Liang, X. Xiao, C. Zhou, G. Chen, Y. Huo, and Y. Wu, Magnetic stripe domains of $[Pt/Co/Cu]_{10}$ multilayer near spin reorientation transition, AIP Advances **6**, 056109 (2016).
[20] S. Bandiera, R. Sousa, B. Rodmacq, L. Lechevallier, and B. Dieny, Effect of a cu spacer between co and pt layers on the structural and magnetic properties in $(Co/Cu/Pt)_5/Pt$ type multilayers, Journal of Physics D: Applied Physics **46**, 485003 (2013).
[21] I. Benguettat-El Mokhtari, A. Mourkas, P. Ntetsika, I. Panagiotopoulos, Y. Roussigné, S. Cherif, A. Stashkevich, F. Kail, L. Chahed, and M. Belmeguenai, Interfacial Dzyaloshinskii-Moriya interaction, interface-induced damping and perpendicular magnetic anisotropy in Pt/Co/W based multilayers, Journal of Applied Physics **126**, 133902 (2019).
[22] S. K. Jena, R. Islam, E. Milińska, M. M. Jakubowski, R. Minikayev, S. Lewińska, A. Lynnyk, A. Pietruczik, P. Aleszkiewicz, C. Autieri, *et al.*, Interfacial Dzyaloshinskii-Moriya interaction in the epitaxial W/Co/Pt multilayers, Nanoscale **13**, 7685 (2021).
[23] M. Belmeguenai, Y. Roussigne, S. M. Cherif, A. Stashkevich, T. Petrisor, M. Nasui, and M. Gabor, Influence of the capping layer material on the interfacial Dzyaloshinskii-Moriya interaction in Pt/Co/capping layer structures probed by brillouin light scattering, Journal of Physics D: Applied Physics **52**, 125002 (2019).
[24] F. Ajejas, Y. Sassi, W. Legrand, S. Collin, A. Thiaville, J. P. Garcia, S. Pizzini, N. Reyren, V. Cros, and A. Fert, Element-selective modulation of interfacial Dzyaloshinskii-Moriya interaction in Pt|Co|Metal based multilayers, arXiv preprint arXiv:2109.00761 (2021).
[25] M. Lonsky, M.-W. Yoo, Y.-S. Huang, J. Qian, J.-M. Zuo, and A. Hoffmann, Structural and magnetic properties of Pt/Co/Mn-based multilayers, Physical Review Materials **6**, 054413 (2022).
[26] J.-C. Rojas-Sánchez, P. Laczkowski, J. Sampaio, S. Collin, K. Bouzehouane, N. Reyren, H. Jaffrès, A. Mougin, and J.-M. George, Perpendicular magnetization reversal in $Pt/[Co/Ni]_3/Al$ multilayers via the spin hall effect of Pt, Applied Physics Letters **108**, 082406 (2016).
[27] S. Karayev, P. D. Murray, D. Khadka, T. Thapaliya, K. Liu, and S. Huang, Interlayer exchange coupling in Pt/Co/Ru and Pt/Co/Ir superlattices, Physical Review Materials **3**, 041401 (2019).
[28] L. Liu, X. Zhao, W. Liu, Y. Song, X. Zhao, and Z. Zhang, Influence of rare earth metal ho on the interfacial Dzyaloshinskii-Moriya interaction and spin torque efficiency in Pt/Co/Ho multilayers, Nanoscale **12**, 12444 (2020).
[29] S. Cheng, B. Wang, I. Lyalin, N. Bagués, A. J. Bishop, D. W. McComb, and R. K. Kawakami, Atomic layer epitaxy of kagome magnet Fe_3Sn_2 and Sn-modulated heterostructures, APL Materials **10**, 061112 (2022).
[30] I. M. Billas, A. Chatelain, and W. A. de Heer, Magnetism from the atom to the bulk in iron, cobalt, and nickel clusters, Science **265**, 1682 (1994).
[31] M. Bersweiler, K. Dumesnil, D. Lacour, and M. Hehn, Impact of buffer layer and pt thickness on the interface structure and magnetic properties in (Co/Pt) multilayers, Journal of Physics: Condensed Matter **28**, 336005 (2016).
[32] W. Zeper, F. Greidanus, P. Carcia, and C. Fincher, Perpendicular magnetic anisotropy and magneto-optical kerr effect of vapor-deposited Co/Pt-layered structures, Journal of Applied Physics **65**, 4971 (1989).
[33] A. Barman, S. Wang, O. Hellwig, A. Berger, E. E. Fullerton, and H. Schmidt, Ultrafast magnetization dynamics in high perpendicular anisotropy $[Co/Pt]_n$ multilayers, Journal of Applied Physics **101**, 09D102 (2007).
[34] X. Wang, Y. Wei, K. He, Y. Liu, Y. Huang, Q. Liu, J. Wang, and G. Han, Effect of the repeat number and co layer thickness on the magnetization reversal process in $[Pt/Co(x)]_N$ multilayers, Journal of Physics D: Applied Physics **53**, 215001 (2020).
[35] X. Wang, A. Cao, S. Li, J. Tang, A. Du, H. Cheng, Y. Sun, H. Du, X. Zhang, and W. Zhao, Manipulating

density of magnetic skyrmions via multilayer repetition and thermal annealing, Physical Review B **104**, 064421 (2021).

[36] B. Wang, P.-k. Wu, N. Bagués Salguero, Q. Zheng, J. Yan, M. Randeria, and D. W. McComb, Stimulated nucleation of skyrmions in a centrosymmetric magnet, ACS Nano **15**, 13495 (2021).

[37] M. J. Benitez, A. Hrabec, A. P. Mihai, T. A. Moore, G. Burnell, D. McGrouther, C. H. Marrows, and S. McVitie, Magnetic microscopy of topologically protected homochiral domain walls in an ultrathin perpendicularly magnetized Co film, arXiv preprint arXiv:1503.07668 (2015).

[38] B. Wang, N. Bagués, T. Liu, R. K. Kawakami, and D. W. McComb, Extracting weak magnetic contrast from complex background contrast in plan-view fege thin films, Ultramicroscopy **232**, 113395 (2022).

[39] R. Juge, N. Sisodia, J. U. Larrañaga, Q. Zhang, V. T. Pham, K. G. Rana, B. Sarpi, N. Mille, S. Stanescu, R. Belkhou, *et al.*, Skyrmions in synthetic antiferromagnets and their nucleation via electrical current and ultrafast laser illumination, Nature Communications **13**, 4807 (2022).

[40] A. Vansteenkiste, J. Leliaert, M. Dvornik, M. Helsen, F. Garcia-Sanchez, and B. Van Waeyenberge, The design and verification of MuMax3, AIP advances **4**, 107133 (2014).

[41] H. Jia, B. Zimmermann, M. Hoffmann, M. Sallermann, G. Bihlmayer, and S. Blügel, Material systems for FM-/AFM-coupled skyrmions in Co/Pt-based multilayers, Physical Review Materials **4**, 094407 (2020).

[42] X. Wang, H. Yuan, and X. Wang, A theory on skyrmion size, Communications Physics **1**, 31 (2018).

Room-Temperature Magnetic Skyrmions in Pt/Co/Cu Multilayers

Shuyu Cheng,[1] Núria Bagués,[2] Camelia M. Selcu,[1,*] Jacob B. Freyermuth,[1] Ziling Li,[1] Binbin Wang,[2] Shekhar Das,[1] P. Chris Hammel,[1] Mohit Randeria,[1] David W. McComb,[2,†] and Roland K. Kawakami[1,‡]

[1] *Department of Physics, The Ohio State University, Columbus, Ohio 43210, United States*

[2] *Department of Materials Science and Engineering, The Ohio State University, Columbus, Ohio 43210, United States*

* selcu.1@osu.edu

† mccomb.29@osu.edu

‡ kawakami.15@osu.edu

CONTENTS

S1. MOKE hysteresis loops of the [Pt/Co/Cu] multilayers

The structures and magnetic properties of $[Pt(2)/Co(t_{Co})/Cu(2)]_N$ sample series are summarized in Table. S1 (replica of Table. 1 in the main text). Fig. S1 shows the MOKE hysteresis loops of $[Pt(2)/Co(t_{Co})/Cu(2)]_N$ samples with strong easy-axis anisotropy (sample I, II, IV, V). Fig. S2 shows the MOKE hysteresis loops of $[Pt(2)/Co(t_{Co})/Cu(2)]_N$ samples with easy-plane anisotropy (sample VII, IX, X). Fig. S3 shows the MOKE hysteresis loops of $[Pt(2)/Co(t_{Co})/Cu(2)]_N$ samples that host skyrmions (sample III, VI, VIII).

Sample ID	Co thickness t_{Co}	Number of periods N	Anisotropy
I	4	5	OOP
II	5	5	OOP
III	6	5	OOP (near SRT)
IV	7	3	OOP
V	7	4	OOP
VI	7	5	OOP (near SRT)
VII	7	7	IP
VIII	8	4	OOP (near SRT)
IX	8	5	IP
X	9	5	IP

TABLE S1. Summary of the structures and magnetic properties of the samples. This is a replica of Table. 1 in the main text.

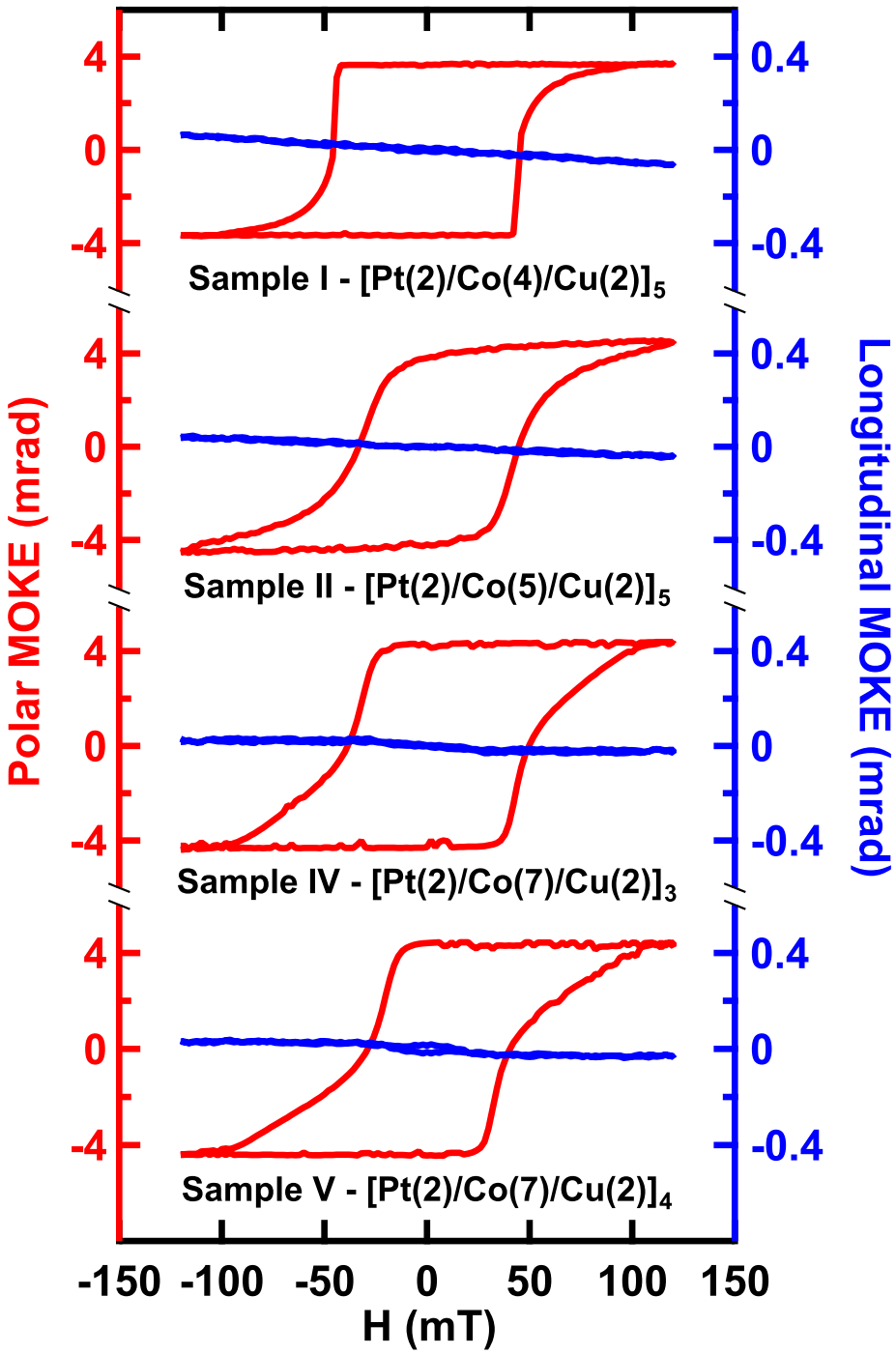

FIG. S1. Polar (red) and longitudinal (blue) MOKE hysteresis loops of [Pt/Co/Cu] multilayers with strong easy-axis anisotropy.

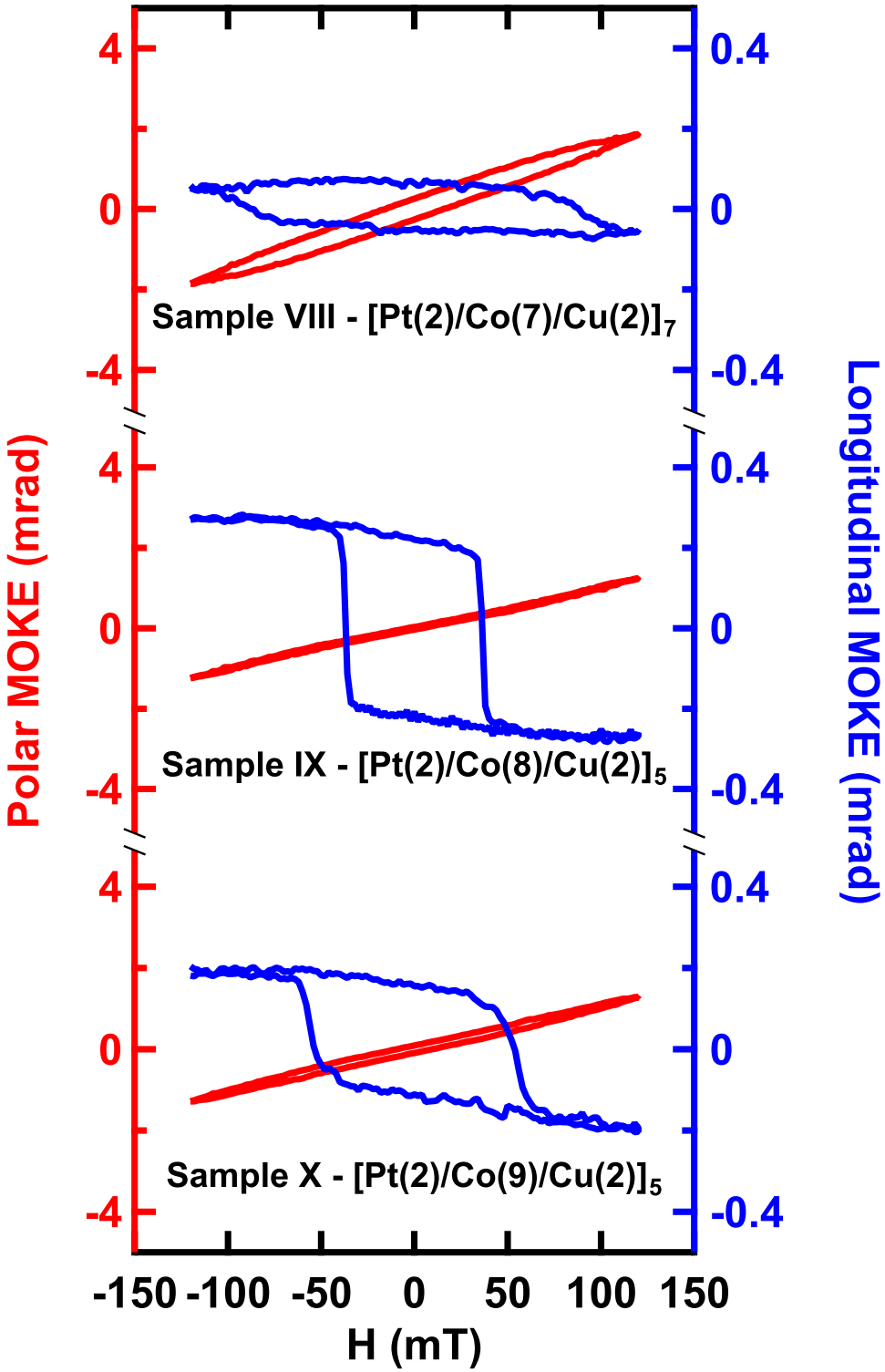

FIG. S2. Polar (red) and longitudinal (blue) MOKE hysteresis loops of [Pt/Co/Cu] multilayers with easy-plane anisotropy.

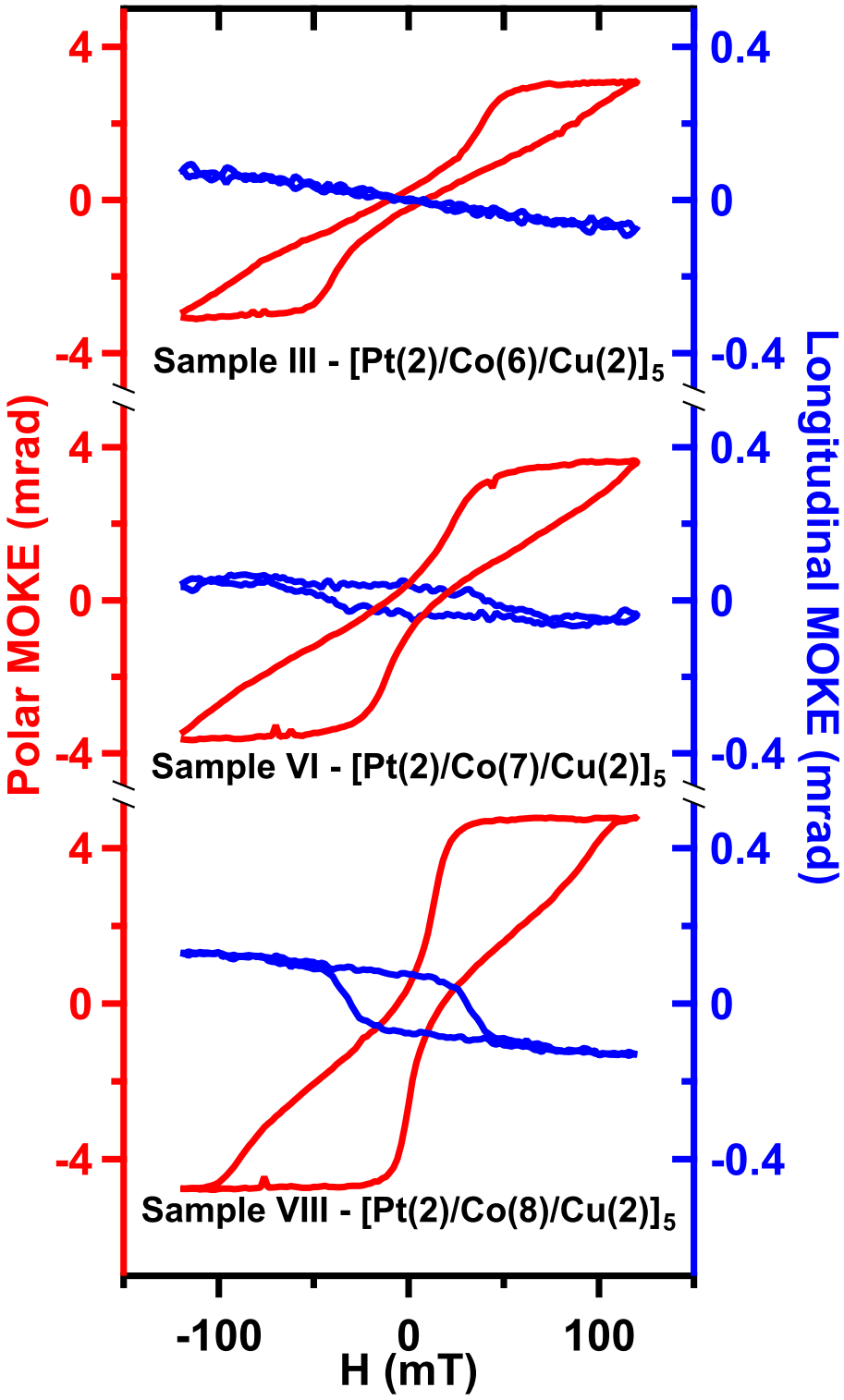

FIG. S3. Polar (red) and longitudinal (blue) MOKE hysteresis loops of [Pt/Co/Cu] multilayers that host skyrmions.

S2. SQUID data of the [Pt/Co/Cu] multilayers

We performed SQUID measurements on $[Pt(2)/Co(7)/Cu(2)]_5$ (sample VI) and $[Pt(2)/Co(8)/Cu(2)]_4$ (sample VIII), which are the two samples that host skyrmions. The out-of-plane (red) and in-plane (blue) hysteresis loops of $[Pt(2)/Co(7)/Cu(2)]_5$ (sample VI) and $[Pt(2)/Co(8)/Cu(2)]_4$ (sample VIII) are shown in Fig. S4a and S4b, respectively.

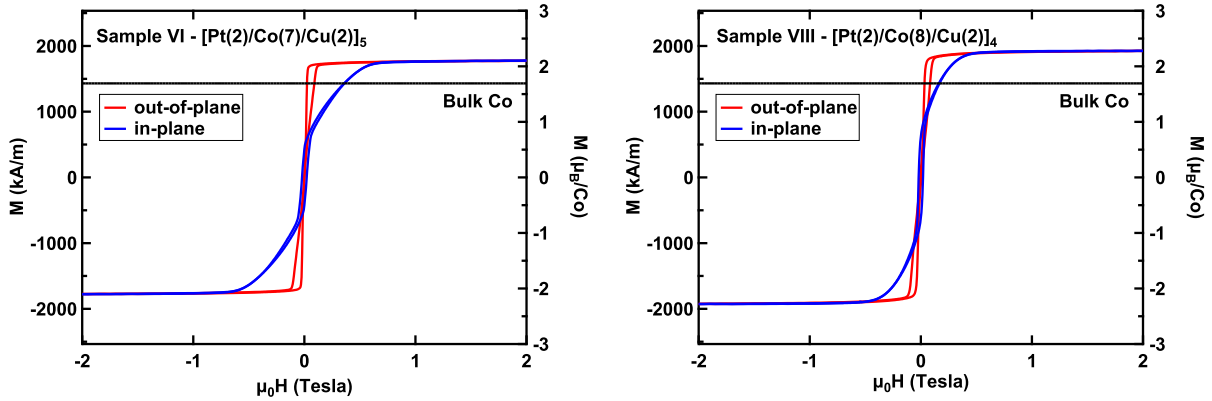

(a) (b)

FIG. S4. SQUID data of (a). $[Pt(2)/Co(7)/Cu(2)]_5$ (sample VI) and (b). $[Pt(2)/Co(8)/Cu(2)]_4$ (sample VIII), respectively. The black solid line represents 1430 kA/m, which is the saturation magnetization of bulk Co.

S3. Additional MFM images

We performed additional MFM measurements on $[Pt(2)/Co(7)/Cu(2)]_5$ sample, as shown in Fig. S5. We started from zero field and ramped up the field up to 100 mT gradually. Similar to $[Pt(2)/Co(8)/Cu(2)]_4$ sample sample, the magnetic textures were dominated by labyrinth domains at 70 mT (Fig. S5a). At 80 mT, the magnetic textures remained mostly unchanged as compared to 70 mT (Fig. S5b). However, as the field was ramped up to 100 mT, a huge portion of labyrinth domains broke into skyrmions or disappeared, as shown in Fig. S5c. This measurement demonstrates the existence of skyrmions in $[Pt(2)/Co(7)/Cu(2)]_5$ sample.

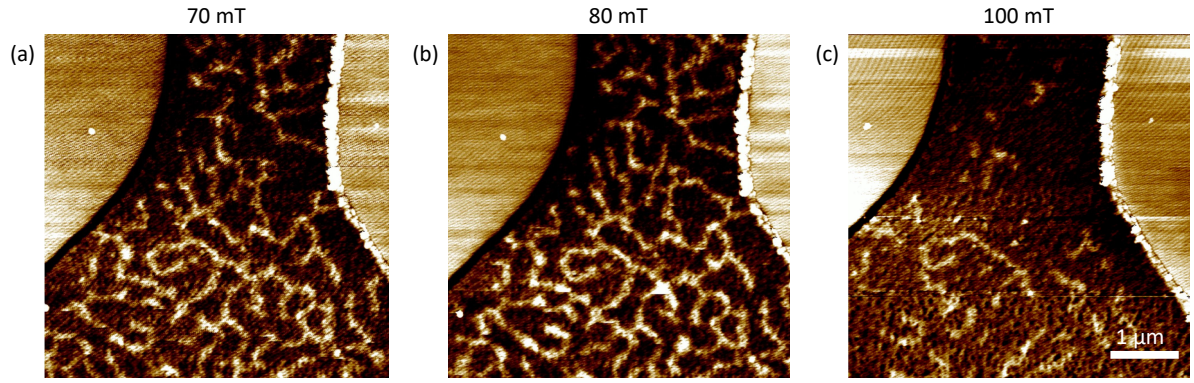

FIG. S5. MFM images of $[Pt(2)/Co(7)/Cu(2)]_5$ sample with magnetic field ramped to (a) 70 mT, (b) 80 mT, and (c) 100 mT.

S4. DETERMINATION OF PARAMETERS FOR MICROMAGNETIC SIMULATIONS

We consider the $[\mathrm{Pt}(2)/\mathrm{Co}(6)/\mathrm{Cu}(2)]_5$ sample described in the main text. The saturation magnetization and magnetic anisotropy are determined from SQUID magnetometry, shown in Figure 2b of the main text. Taking into account the thickness of the sample and contribution of the 5 nm Pt buffer layer, the saturation magnetization is found to be M_S=821 kA/m. The in-plane and out-of-plane saturation fields in the SQUID measurement can be used to find the effective anisotropy, which combines the magnetic anisotropy described by K_u and the shape anisotropy of the sample. The relationship between the effective anisotropy K_{eff} and the magnetic anisotropy K_u is given by:

$$K_{eff} = K_u - \frac{1}{2}\mu_0 M_S^2 \tag{S1}$$

Using this relationship, we find the magnetic anisotropy to be K_u=608.5 kJ/m^3.

Next, we determine the exchange stiffness A_{ex}. The usual way to measure the exchange stiffness is through measuring the transition temperature T_C of the material. However, the transition temperature in this material is above 400 K, which is the maximum temperature that can be applied in the experiment. However, we know the exchange stiffness for bulk cobalt, A_{ex}=11 pJ/m, which serves as an upper bound on the T_C of our material. Since the thin film will have a lower T_C than the bulk, the exchange stiffness will be lower accordingly. There is also a relationship between exchange stiffness and skyrmion size, with larger stiffness leading to larger skyrmions. Since the skyrmions seen in the experiment are quite large, the exchange stiffness will be close to the value for bulk cobalt, and the simulations suggest a value of A_{ex}=10 pJ/m.

To try to understand the skyrmion size as a function of magnetic field and the strength of the DMI in the material, we performed micromagnetic simulations using MuMax3 [**?**]. We found for a given value of DMI, the skyrmion size decreases as magnetic field increases, whereas for a given magnetic field, increasing the strength of the DMI increases the size of the skyrmion. To understand this, we use the skyrmion ansatz of Wang *et al.* [**?**] from their theory paper on skyrmion size. Our simulation results agree with their findings, that the skyrmion radius increases with DMI strength and decreases with magnetic field strength.